The Astrophysical Journal, 747:142 (15pp), 2012 March 10 doi:10.1088/0004-637X/747/2/142

HIGH-RESOLUTION SPECTROSCOPY OF Ne II EMISSION FROM YOUNG STELLAR OBJECTS*

G. G. Sacco[1,7], E. Flaccomio[2], I. Pascucci[3], F. Lahuis[4], B. Ercolano[5], J. H. Kastner[1], G. Micela[2], B. Stelzer[2], and M. Sterzik[6]

[1] Chester F. Carlson Center for Imaging Science, Rochester Institute of Technology, Rochester, NY 14623, USA; gsacco@arcetri.inaf.it
[2] INAF-Osservatorio Astronomico di Palermo, Palermo 90143, Italy
[3] Department of Planetary Sciences, University of Arizona, Tucson, AZ 85721, USA
[4] SRON Netherlands Institute for Space Research, P.O. Box 800, 9700 AV Groningen, The Netherlands
[5] Ludwig-Maximilians-Universitaet University Observatory, Munich D-81679, Muenchen, Germany
[6] European Southern Observatory, Casilla 19001, Santiago 19, Chile
Received 2011 October 25; accepted 2011 December 21; published 2012 February 24

ABSTRACT

Constraining the spatial and thermal structure of the gaseous component of circumstellar disks is crucial for understanding star and planet formation. Models predict that the [Ne II] line at 12.81 μm detected in young stellar objects (YSOs) with *Spitzer* traces disk gas and its response to high-energy radiation, but such [Ne II] emission may also originate in shocks within powerful outflows. To distinguish between these potential origins for mid-infrared [Ne II] emission and to constrain disk models, we observed 32 YSOs using the high-resolution ($R \sim 30{,}000$) mid-infrared spectrograph VISIR at the Very Large Telescope. We detected the 12.81 μm [Ne II] line in 12 objects, tripling the number of detections of this line in YSOs with high spatial and spectral resolution spectrographs. We obtain the following main results. (1) In Class I objects the [Ne II] emission observed from *Spitzer* is mainly due to gas at a distance of more than 20–40 AU from the star, where neon is, most likely, ionized by shocks due to protostellar outflows. (2) In transition and pre-transition disks, most of the emission is confined to the inner disk, within 20–40 AU from the central star. (3) Detailed analysis of line profiles indicates that, in transition and pre-transition disks, the line is slightly blueshifted (2–12 km s^{-1}) with respect to the stellar velocity, and the line width is directly correlated with the disk inclination, as expected if the emission is due to a disk wind. (4) Models of EUV/X-ray-irradiated disks reproduce well the observed relation between the line width and the disk inclination, but underestimate the blueshift of the line.

Key words: circumstellar matter – infrared: stars – line: profiles – protoplanetary disks – stars: formation

Online-only material: color figures

1. INTRODUCTION

Disks orbiting young stars (1–10 Myr) are sources of accreting material and sites of nascent planetary systems. Observations that can establish the physical conditions and evolution of the gaseous component within young circumstellar disks are essential if we are to understand the magnetospheric accretion processes that determine a star's zero-age main-sequence mass, protoplanetary disk structure and evolution, and the processes involved in planet formation. Despite their relevance to all of these important open issues, the physical and chemical properties of gaseous circumstellar disks are still poorly understood. Submillimeter observations of molecular lines provide insight into the chemistry and the physics of the outer disk regions ($r > 100$ AU; e.g., Dutrey et al. 1994, 1997; Kastner et al. 1997, 2008), but the properties of the gas within 20–30 AU have only recently been investigated thanks to the mid-infrared IRS spectrograph on board the *Spitzer Space Telescope*, e.g., by the discovery of emission lines from several species including organic molecules and water (Carr & Najita 2008; Salyk et al. 2008).

One of the most interesting mid-infrared spectral features is the [Ne II] line at 12.81 μm (Pascucci et al. 2007; Lahuis et al. 2007; Espaillat et al. 2007b; Flaccomio et al. 2009; Güdel et al. 2010). The importance of the [Ne II] line is twofold: it traces warm gas ($T \sim 5000$ K) and, due to the high first ionization potential of neon (21.56 eV), it is a good proxy for the influence of stellar extreme ultraviolet (EUV) and X-ray radiation on the disk. The presence of strong [Ne II] emission at 12.81 μm from protoplanetary disks was first predicted by Glassgold et al. (2007), who suggested that neon is ionized by K-shell absorption of X-ray photons at energy $E > 0.9$ keV. This hypothesis has been refined by sophisticated irradiated disk models (Meijerink et al. 2008; Ercolano et al. 2008; Ercolano & Owen 2010), which predict a correlation between the stellar X-ray luminosity and the total [Ne II] line luminosity. It has also been suggested that X-rays may determine disk dissipation by heating the circumstellar gas to temperatures $T \sim 10^3$–10^4 K and triggering its photoevaporation (Ercolano et al. 2008; Ercolano & Owen 2010; Owen et al. 2010). Neon ionization and disk photoevaporation could also be induced by EUV photons produced by accretion shocks (Hollenbach & Gorti 2009; Alexander 2008). However, EUV photons are more easily absorbed by neutral hydrogen, so they are less likely than X-rays to reach and affect the circumstellar disk, especially early in the Class II phase when inflow and outflow from the inner disk are densest (Ercolano et al. 2009; Owen et al. 2010).

A detailed comparison between models and observations is required to clarify this complex theoretical scenario. Several surveys of the [Ne II] emission from young stellar objects (YSOs) have been carried out in the last 5 years using low spectral and spatial resolution data obtained with *Spitzer*/Infrared

* Based on observations collected at the European Organisation for Astronomical Research in the Southern Hemisphere, Chile, with the mid-infrared spectrograph and imager VISIR (Program IDs 083.C-0883, 084.C-0211, and 085.C-0860).
[7] Current address: INAF-Osservatorio Astrofisico di Arcetri, Largo E. Fermi 5, Firenze 50125, Italy.

Spectrograph (IRS; Pascucci et al. 2007; Espaillat et al. 2007b; Lahuis et al. 2007; Flaccomio et al. 2009; Güdel et al. 2010). A weak correlation between X-ray and [Ne II] luminosity has been found by Güdel et al. (2010), who investigated a sample consisting of 92 pre-main-sequence stars. Furthermore, [Ne II] emission was found to be stronger in Class I YSOs and in sources driving protostellar jets than in more evolved YSOs (Flaccomio et al. 2009; Güdel et al. 2010). The strong [Ne II] emission observed in embedded YSOs driving jets—orders of magnitude larger than predicted by models of emission from disks—is unlikely produced by irradiated gas within the inner disk, but it may be produced either by shocks, in the circumstellar envelope or in protostellar jets (Hollenbach & Gorti 2009), or in the launching region of magnetically driven outflows irradiated by stellar X-ray emission (Shang et al. 2010).

The *Spitzer*/IRS data, with their limited spectral and spatial resolution, provide limited information on the velocity and the spatial structure of the emitting gas. High spectral and spatial resolution observations of the [Ne II] line from the ground can be used to decouple disk and jet emission. For example, using Very Large Telescope (VLT)/VISIR, clear evidence of [Ne II] emission from protostellar jets has been discovered in the triple system T Tau (van Boekel et al. 2009). The observations show that the predominant [Ne II] emission component is shifted to a velocity compatible with the jet motion and is extended ($\sim$1.″1) along the jet direction. However, a disk origin for the [Ne II] emission has been suggested by high spectral resolution observations of the nearby classical T Tauri stars TW Hya (Herczeg et al. 2007), AA Tau, and GM Tau (Najita et al. 2009). In all of these stars the line appeared broadened (Δv = 21–70 km s^{-1}) and centered near the stellar velocity. The absence of detectable blueshift suggested that the emission is produced from a static disk atmosphere, but given the low signal-to-noise ratio of this data, it was not possible to rule out the presence of emission from a slow (v = 1–10 km s^{-1}) photoevaporative wind.

Evidence of [Ne II] emission arising from both a protostellar jet and a photoevaporative disk wind has been found by Pascucci & Sterzik (2009), who observed four optically thick disk objects (Sz 73, Sz 102, HD 3700A, and VW Cha) and three transition disk objects (TW Hydrae, T Cha, and CS Cha). Transition disk objects have no excess in the near-infrared and a strong excess in the far-infrared, which is interpreted as a signature of a few AU central gap within the disk (see Williams & Cieza 2011, and references therein). Pascucci & Sterzik (2009) detected [Ne II] emission from all the transition disk objects, finding the line slightly blueshifted ($\Delta v \sim$ 4–6 km s^{-1}) and broadened, with a line width correlated with inclination angle. These characteristics appear consistent with model profiles expected from a photoevaporative disk wind triggered by EUV or X-ray stellar emission (Alexander 2008; Ercolano & Owen 2010), but a larger number of analogous observations are required to confirm their results. They detected the emission in only one of the optically thick disk objects, Sz 73. Since the emission is strongly blueshifted (Δv = 100 km s^{-1}) and broadened (Δv = 60 km s^{-1}), an origin from fast outflowing material is more likely than a disk origin. Additional evidence for a photoevaporative wind comes from the asymmetric [Ne II] line profile detected toward the transition disk around TW Hydrae (Pascucci et al. 2011).

With the aim of understanding the origin of the [Ne II] emission from stars at various evolutionary stages and with different circumstellar characteristics and to test X-ray- and EUV-irradiated disk models with observations, we performed a high-resolution spectroscopic survey of the [Ne II] emission from 32 T Tauri stars and YSOs spanning a range of spectral energy distributions (SEDs), with the VISIR spectrograph at the VLT. Here, we present the results of this survey, including a comparison with *Spitzer*/IRS spectra, some of which are published here for the first time. In Section 2, we describe the observed sample, the observations, and the data reduction procedure; in Section 3, we report the results of analysis of the VISIR and the *Spitzer* data; in Section 4, we discuss our results and compare them with the predictions of irradiated disk models; and in Section 5, we draw our conclusions.

2. OBSERVATIONS AND DATA REDUCTION

We observed 32 T Tauri stars and YSOs (two resolved binaries IRS 43 and CrA IRS5 are counted as four) belonging to several star-forming regions and young stellar associations. In Section 2.1, we describe the properties of the observed stars and the procedures used to observe them; in Section 2.2, we describe the data reduction process.

2.1. Target Sample and Observations

All the stars in our sample, with the exception of IRAS 08267-3336, are closer than 150 pc. We include stars from both very young star-forming regions such as ρ Oph and Corona Australis (1–3 Myr), which are characterized by a large number of deeply embedded protostellar objects, and older stellar associations like ϵ Cha and β Pictoris (6–12 Myr) that are mainly composed of apparently diskless (Class III) stars. We consider different regions and associations to include in our sample YSOs of different infrared classes. Furthermore, we gave higher priority to YSOs with *Spitzer* detections of the [Ne II] emission at 12.81 μm. Two objects (T Cha and Sz 73)—whose [Ne II] line was already detected with VLT/VISIR by Pascucci & Sterzik (2009)—have been observed again to investigate the variability of the emission.

The full list of the observed targets is reported in Table 1, where we list object coordinates from the Two Micron All Sky Survey (2MASS) catalog (Skrutskie et al. 2006), parent region, distance (based on the parent region and data reported in the literature), heliocentric radial velocities, infrared class, disk inclination, X-ray luminosity in the band 0.3–10.0 keV,[8] and mass accretion rate. All data in Table 1 are retrieved from the literature. Radial velocities for some of the stars in the ρ Oph and Corona Australis star-forming regions were not available in the literature, so these radial velocities have been estimated from the velocity of the parent cloud or nearby stars (see Table 1 for further details). Disk inclinations reported in Table 1 are derived by different techniques. Specifically, in eight YSOs, disk inclinations are derived from interferometric submillimeter observations or scattered-light imaging of the disk (with estimated uncertainties 5°–10°). For RU Lupi we assumed the disk inclination to be equal to the inclination of the stellar rotation axes (error $\sim$10°), and for T Cha and RX J1615.3-3255 we report the inclination derived from a fit of the SED. Errors on the inclination derived from the SED are probably much higher. However, in the case of T Cha (inclination angle 75°) other observational signatures—e.g., a highly variable optical extinction—demonstrate the presence of

[8] Some published L_X values are for slightly different bands and were corrected to account for the band differences.

Table 1
Observed targets

Star	R.A.	Decl.	Region	d (pc)	$v_{\rm Helio}$ (km s^{-1})	Class	Inclination (deg)	L_X[i] (10^{29} erg s^{-1})	$\dot{M}_{\rm acc}$ ($M_\odot$ yr^{-1})	References
V807 Tau	4:33:06.64	24: 9:55.0	Taurus	140	...	Class II	...	...	...	1 - 2 - - -
LkCa 15	4:39:17.80	22:21:03.5	Taurus	140	17.0 ± 1.2	pTr	42[e]	...	−8.6	1 3 4 4 - 4
IRAS 08267-3336	8:28:40.70	−33:46:22.2	Gum Nebula	450	...	Class II	...	230.0	...	5 - 5 - 6 -
Hen 3-600 A	11:10:27.88	−37:31:52.0	TW Hya	39	15.6 ± 0.2	Tr	36[e]	3.0	−9.7	7 8 9 10 11 12
WX Cha	11:09:58.74	−77:37:08.9	Cha I	178	...	Class II	...	46.0	...	6 - 13 - 6 -
XX Cha	11:11:39.66	−76:20:15.3	Cha I	178	...	Class II	...	11.0	...	6 - 13 - 6 -
T Cha	11:57:13.49	−79:21:31.4	ϵ Cha	109	14.0 ± 1.3	Tr	75[f]	30.0	−8.4	8 14 15 16 6 16
MP Mus	13:22:07.53	−69:38:12.2	ϵ Cha	103	11.6 ± 0.2	pTr	30[g]	14.6	−9.1	8 8 17 18 19 12
IM Lupi	15:56:09.22	−37:56:05.8	Lupus 2	150	...	Class II	50[g]	37.0	...	20 - 21 21 6 -
SZ 73	15:47:56.94	−35:14:34.7	Lupus 1	150	-3.3 ± 2.5	Class II	...	...	...	20 22 23 - - -
RU Lupi	15:56:42.30	−37:49:15.4	Lupus 2	150	-1.9 ± 0.2	ClassII/Jet	10[h]	10.0	−7.7	20 24 25/26 24 6 12
RX J1615.3-3255	16:15:20.23	−32:55:05.1	Lupus	150	-2.4 ± 1.0	Tr	5[f]	...	...	20 27 28 28 - -
SSTc2dJ162145.1[a]	16:21:45.13	−23:42:31.6	ρ Oph	120	-6.3 ± 1.7[b, c]	Class I	...	...	...	29 30 31 - - -
DoAr 25/GY92 17	16:26:23.68	−24:43:13.9	ρ Oph	120	-6.3 ± 1.7[b, c]	Class II	59[e]	18.6	−7.6	29 30 32 33 32 32
WL 10/GY92 211	16:27:09.11	−24:34:08.1	ρ Oph	120	-6.3 ± 1.7[b, c]	Class II	...	4.0	−7.9	29 30 32 - 32 32
Elias 29/GY92 214	16:27:09.43	−24:37:18.7	ρ Oph	120	-6.3 ± 1.7[b, c]	Class I	...	16.0	−7.0	29 30 32 - 32 32
SR 21	16:27:10.28	−24:19:12.7	ρ Oph	120	-6.3 ± 1.7[b, c]	Tr	22[e]	...	8.8	29 30 34 33 - 35
WL 19	16:27:11.71	−24:38:32.1	ρ Oph	120	-6.3 ± 1.7[b, c]	pTr	...	75.5	9.0	29 30 32 - 32 32
WL 20/GY92 240	16:27:15.88	−24:38:43.4	ρ Oph	120	-6.3 ± 1.7[b, c]	Class II	...	11.6	−7.9	29 30 32 - 32 32
IRS 43/GY92 265	16:27:26.94	−24:40:50.8	ρ Oph	120	-7.2 ± 1.5[d]	Class I	...	27.7	−7.1	29 36 32 - 32 32
IRS 44/GY92 269	16:27:28.03	−24:39:33.5	ρ Oph	120	-5.8 ± 1.5[d]	Class I	...	24.2	−6.1	29 36 32 - 32 32
IRS 45/GY92 273	16:27:28.44	−24:27:21.0	ρ Oph	120	-3.1 ± 1.5[b, c]	Class II	...	0.7	9.0	29 36 32 - 32 32
IRS 47/GY92 279	16:27:30.18	−24:27:43.4	ρ Oph	120	-3.1 ± 1.5[d]	Class II	...	1.9	−8.4	29 36 32 - 32 32
IRS 60/WSB 71a	16:31:30.88	−24:24:40.0	ρ Oph	120	-6.3 ± 1.7[b, c]	Class II/Jet	...	...	...	29 32 36/37 - - -
DoAr 44	16:31:33.46	−24:27:37.3	ρ Oph	120	-6.3 ± 1.7[b, c]	pTr	45[e]	...	...	29 30 38/33 33 - -
V4046 Sgr	18:14:10.48	−32:47:34.4	β Pic	73	-6.9 ± 0.2	Tr	35[e]	12.0	−9.2	39 40 41 42 43 12
RX J1842.9-3532	18:42:57.98	−35:32:42.7	CrA	130	1.2 ± 1.0	Tr	...	...	−9.0	44 44 45 - - 6
CrA IRS5	19:01:48.02	−36:57:22.4	CrA	130	1.0 ± 1.0	Class I/Jet	...	30.3	...	46 46 47/48 - 4
R CrA 7B	19:01:56.39	−36:57:28.4	CrA	130	1.0 ± 1.0	Class 0/I	...	4.0	...	46 46 47 - 47 -
T CrA	19:01:58.78	−36:57:49.9	CrA	130	1.0 ± 1.0	Class II/Jet	...	0.1	...	46 46 47/48 - 47 -

Notes. Stellar coordinates are retrieved from the 2MASS catalog (Skrutskie et al. 2006), except for CrA IRS5 and R CrA 7B (Forbrich & Preibisch 2007).
[a] Full stellar name SSTc2dJ162145.13-234231.6.
[b] Mean radial velocity of 10 members of the ρ Oph star-forming region measured by Doppmann et al. (2003).
[c] The heliocentric velocity has been derived from the velocity with respect to the local standard of rest using the IRAF task rvcorrect.
[d] Assumed equal to the radial velocity of IRS 47.
[e] Measured by submillimeter interferometric observations of the disk.
[f] Derived from the fit of the SED.
[g] Measured by scattered-light imaging of the disk.
[h] Assumed equal to the inclination of the stellar rotation axes.
[i] Unabsorbed X-ray luminosity in the range 0.3–10 keV.
References. (1) Kenyon et al. 1994; (2) Furlan et al. 2009; (3) Hartmann et al. 1987; (4) Espaillat et al. 2007a; (5) Pettersson 2008; (6) Güdel et al. 2010; (7) Kastner et al. 1997; (8) Torres et al. 2006; (9) Uchida et al. 2004; (10) Andrews et al. 2010; (11) Huenemoerder et al. 2007; (12) Curran et al. 2011; (13) Manoj et al. 2011; (14) Guenther et al. 2007; (15) Brown et al. 2007; (16) Schisano et al. 2009; (17) Cortes et al. 2009; (18) Kastner et al. 2010; (19) Argiroffi et al. 2009; (20) Comerón 2008; (21) Pinte et al. 2008; (22) Melo 2003; (23) Hughes et al. 1994; (24) Stempels & Piskunov 2002; (25) Schegerer et al. 2009; (26)Takami et al. 2001 (27) Wichmann et al. 1999; (28) Merín et al. 2010; (29) Lombardi et al. 2008; (30) Doppmann et al. 2003; (31) Flaccomio et al. 2009; (32) Andrews et al. 2009; (33) Eisner et al. 2009; (34) Natta et al. 2006; (35) Covey et al. 2006; (36) Evans et al. 2009; (37) Wu et al. 2002; (38) Espaillat et al. 2010; (39) Torres et al. 2008; (40) Quast et al. 2000; (41) Schütz et al. 2009; (42) Kastner et al. 2008; (43) Argiroffi et al. 2011; (44) Neuhäuser et al. 2000; (45) Neuhäuser & Forbrich 2008; (46) Hughes et al. 2010; (47) Forbrich & Preibisch 2007; (48) Wang et al. 2004.

a circumstellar disk seen nearly edge-on. For all the remaining targets, no information on the disk inclinations are available in the literature.

The infrared class of our targets, reported in Table 1, was derived from analyses reported in the literature (references are reported in the last column of Table 1) of the SED in the near-infrared and mid-infrared bands and, in three cases (R CrA-7B, CrA IRS 5, and T CrA), of mid-infrared color–magnitude diagrams. Specifically, we classified, as Class I and Class II, sources with SED slopes in the ranges $\alpha > 0$ and $-2 < \alpha \leqslant 0$, respectively. To first approximation, the slope of the SED indicates the presence of a massive protostellar envelope (in Class I) or an optically thick disk (in Class II). However, recent detailed studies of the dust emission in the mid-infrared and submillimeter band (see Williams & Cieza 2011 for a review) suggest that within the Class II are included stars with an optically thick disk and stars harboring a more evolved disk, characterized by the presence of an inner gap. As pointed out by Pascucci & Sterzik (2009), the origin of the [Ne II] emission in the latter group of stars is much different than in the former, therefore, following the definitions mostly used in the literature, we define two more classes of objects: the transition disks and the pre-transition disks. Specifically, circumstellar disks with signatures of a large (few AU) inner hole—i.e., no excess in the near-infrared and large excess in the mid-infrared—are classified as transition objects (Tr), while circumstellar disks

with an SED indicating the presence of a gap that separates the inner disk from the outer disk are classified as pre-transition disks (pTr; see Espaillat et al. 2007a for a detailed discussion about the difference between transition and pre-transition disks).

On the basis of these criteria, our sample is composed of 9 Class I, 13 Class II, 6 transition disks, and 4 pre-transition disks. However, the information that we found in the literature for our sample were not homogeneous, so we cannot exclude that with a more complete and homogeneous set of data some of the Class II objects may be classified as transition or pre-transition disks.

It is worth noting that a large gap in the dusty component of the disk does not necessarily imply the presence of a gap in its gaseous component, where the [Ne II] emission is produced. For example, in our sample T Cha, V4046 Sgr and Hen 3-600 are transition disk objects but they are also actively accreting, as strong optical emission lines demonstrate (Schisano et al. 2009; Curran et al. 2011). The presence of these accretion signatures indicates that the hole within the dusty component of the disk is filled with gas.

VISIR observations have been carried out during three different ESO observing periods, P83, P84, and P85. We used VISIR (Lagage et al. 2004) in high-resolution, long-slit, spectroscopic mode. The echelle grating is centered on the [Ne II] fine structure line at 12.81355 μm (Yamada et al. 1985) and covers the spectral range between 12.79 and 12.83 μm. We set the slit width at 0.″4 ($\sim$40 AU at a distance of $\sim$100 pc), which coincides with the spatial resolution of the instrument when the visual seeing is better than 0.″6–0.″7 (Smette & Vanzi 2007), and a spectral resolution $R \sim 30{,}000$ ($\sim$10 km s^{-1} in velocity scale). The spectral and spatial resolutions of our observations are, therefore, 50 and 10 times higher than [Ne II] observations carried out using IRS spectrograph on board *Spitzer*, respectively ($R \sim 600$ and slit width $\sim$4.″7). For flux calibration and telluric correction, we observed a standard star immediately before and/or after the observation of each target at airmass as close as possible to that of the target. The observation of stars requiring long exposure times have been split in more than one segment, alternating an observation of the target with an observation of the standard star. Table 2 reports date, time, airmass, and exposure time of all the observed stars and their associated standard stars. During the first run, we also observed the asteroid Kalliope to obtain a pure sky absorption spectrum, and Titan to verify the instrument resolution. Our Titan spectrum has been analyzed by Pascucci et al. (2011), who measured the full width at half-maxima (FWHM) and the centroid position of unresolved lines of C_2H_2 and C_2H_6. The measured FWHM span a very narrow range with a mean value of 10 km s^{-1}, as expected considering the instrument resolution, while the uncertainties on the line centroids is $\sim$1 km s^{-1}. However, by tests on a set of standard stars and from TW Hydrae data, Pascucci et al. (2011) found that the absolute accuracy of the line centroid is 2 km s^{-1} due to uncertainties in placing the source in the center of the slit.

We also compiled fluxes in the [Ne II] lines measured from *Spitzer*/IRS (Werner et al. 2004; Houck et al. 2004) from the literature, and when these were not available, we downloaded, reduced, and analyzed data from the *Spitzer* archive. *Spitzer* [Ne II] fluxes are reported in Table 3, together with the results obtained from the VISIR observations, for a direct comparison.

2.2. Data Reduction

We reduced all VLT/VISIR data using the VISIR pipeline version 3.2.2 (Lundin 2008) in conjunction with our IDL scripts. VISIR data are a collection of data cubes, each corresponding to a nod position. Every data cube contains $2n+1$ planes, where n is the number of the chopping cycles. Odd planes contain the images from the on-source chopping cycle (A_i), while the even planes contain the average of the differences between the current and all the previous on-source (A_i) and off-source (B_i) chopping cycle images. Therefore, the last plane contains the average of all the $A_i - B_i$ images.

The first part of the data reduction is executed by the pipeline. Specifically, all the data cubes are coupled in pairs, composed of two complementary nod positions. The last planes of each pair are summed and divided by the total integration time. At this point, because we used standard observing mode in which the chopping and nodding directions and throws are the same, each nodded image contains a double positive beam in the center and a negative beam on each side. To form the final science frame, all the nodded images are added, after bad pixel cleaning and correction of the image distortion. In a small number of cases, we excluded from the final sum some pairs of nod images taken when the background emission was particularly strong and variable, e.g., due to the presence of thin clouds. The standard deviation of the noise in the resulting image is calculated from the dispersion of pixel values, after the rejection of outliers with an iterative sigma-clipping. Pixels with values less than three times the standard deviation of the noise are classified as noisy.

The spectrum is extracted by the pipeline using the method developed by Horne (1986). Specifically, a weight map is generated by collapsing the spectrum along the dispersion direction, normalizing the absolute flux of the one-dimensional image to 1 and setting to zero noisy pixels. The resulting profile is then replicated along the dispersion direction to cover the full frame. The final spectrum is obtained by multiplying the science frame for the weight map and summing along the slit direction. Pixels classified as noisy are used to calculate errors (see Figure 1).

After several tests, we realized that this method for spectrum extraction fails in two situations: (1) when the signal-to-noise ratio is very low and the residual noise is comparable to the signal from the star, because the weight map, and therefore the extracted spectrum, is significantly contaminated by noise (see the middle panels of Figure 1); (2) when we observe a spatially resolved binary with the two components aligned along the slit, because by multiplying the science frame for the weight map and summing along the slit direction we obtain an integrated spectrum of both components, losing information on the emission of each component. To avoid these problems, we extracted the spectra of faint sources and resolved binary systems by defining our own weight map. The weight map for faint sources is the sum of three Gaussians, one centered on the peaks of the positive beam and two centered on the negative beams, with half and opposite amplitudes with respect to the first one (see Figure 1). To separately extract the spectra of each component of the spatially resolved binaries, we defined different maps for each component, using the same method described above (see bottom panels of Figure 1). To check this procedure, we applied this method to the bright stars of our sample, obtaining the same results as with the standard procedure (see top panels of Figure 1).

The wavelength calibration is done by cross-correlating an infrared background spectrum with a synthetic model spectrum of the atmosphere. The infrared background spectrum is extracted from the input files before correcting for chopping and nodding. The whole extraction procedure described above is performed in the same way for both the science target and the

Table 2
Observation Log

Star	Day (yyyy-mm-dd)	U.T. (hh:mm)	Airmass	t_{exp} (s)	Standard	U.T. (hh:mm)	Airmass (s)	t_{exp}
T Cha	2009-06-02	00:01	1.7–1.8	1800	HD 92305	23:05	1.7	360
IRS 43 S	2009-06-02	01:25	1.2–1.3	450	HD 149447	01:02/02:42	1.4/1.1	360 × 2
IRS 43 N	2009-06-02	01:58	1.1–1.2	450	HD 149447	02:42	1.1	360
DoAr 25	2009-06-02	03:09	1.0–1.05	1700	HD 151680	04:35	1.02	360
DoAr 25	2009-06-02	04:44	1.0–1.3	5500	HD 151680	04:35/07:32	1.0/1.2–1.3	360 × 2
IRS 44	2009-06-02	07:50	1.4–1.8	1800	HD 151680	07:32/08:50	1.2–1.3/1.6–1.7	360 × 2
CrA IRS 5	2009-06-02	09:38	1.2–1.4	1800	HD 177716	09:09	1.1	360
Sz 73	2009-06-02	23:46	1.4–1.6	1800	HD 139127	23:20	1.65–1.71	360
WL 10	2009-06-03	01:14	1.0–1.4	3600	HD 151680	00:41/03:53	1.6/1.0	360 × 2
Kalliope	2009-06-03	03:35	1.0–1.1	360	...	...	...	
RX J1842.9-3532	2009-06-03	04:19	1.1–1.2	1800	HD 151680	03:53	1.0	360
WL 10	2009-06-03	05:56	1.0–1.4	3600	HD 151680	07:49	1.3	360
WL 20	2009-06-03	08:08	1.6–2.0	1800	HD 151680	09:02	1.8	360
RX J1842.9-3532	2009-06-03	09:34	1.3–1.7	1800	HD 151680	09:02	1.8	360
Titan	2009-06-03	22:43	1.2	300	...	...	...	
IRS 47	2009-06-03	00:36	1.3–1.6	1800	HD 151680	01:35	1.3	360
IRS 47	2009-06-04	02:01	1.0–1.2	1800	HD 151680	01:35/03:50	1.3/1.0	360 × 2
IRS 45	2009-06-04	04:48	1.0–1.1	3600	HD 151680	03:50/06:32	1.0/1.1	360 × 2
IRS 45	2009-06-04	06:52	1.2–1.7	3600	HD 151680	06:32/08:31	1.1/1.6	360
V4046 Sgr	2009-06-04	08:55	1.3–1.6	2700	HD 169916	10:12	1.6–1.8	600
IRAS 08267-3336	2009-12-15	07:18	1.01–1.02	1980	HD 70555	08:45	1.03-1.06	180
IRAS 08267-3336	2009-12-15	06:12	1.02–1.07	1980	HD 70555	05:48	1.1	180
XX Cha	2010-01-04	06:34	1.7	1980	HD 92305	05:50	1.8	180
WX Cha	2010-01-08	04:48	1.7	1980	HD 92305	05:57	1.7	180
WX Cha	2010-01-08	06:44	1.8–2.0	1980	HD 92305	07:48	1.8	180
XX Cha	2010-01-09	03:58	1.9–2.1	1980	HD 92305	05:02	1.9	180
IM Lupi	2010-01-30	07:48	1.4–1.7	1980	HD 139127	08:51	1.3	180
IM Lupi	2010-01-31	07:54	1.4–1.6	1980	HD 139127	07:20	1.7–1.8	180
MP Mus	2010-06-03	23:18	1.4–1.5	3600	HD 123139	22:53	1.3	360
IRS 44	2010-06-04	01:05	1.2–1.4	1800	HD 151680	02:04	1.2	360
Elias 29	2010-06-04	02:29	1.0–1.1	3600	HD 151680	04:10	1.0	720
DoAr 44	2010-06-04	05:20	1.0–1.2	3600	HD 151680	04:10/07:02	1.0/1.2	720/360
RU Lupi	2010-06-04	07:37	1.5–1.9	3600	HD 150798	08:35	1.8	180
T CrA	2010-06-04	09:22	1.2–1.6	7200	HD 169916	8:52	1.2–1.3	600
Hen 3-600 A	2010-06-04	23:10	1.0–1.1	3600	HD 93813	22:48	1.0	360
SR 21	2010-06-05	01:36	1.0–1.2	3600	HD 151680	03:18	1.2	360
RU Lupi	2010-06-05	03:44	1.0–1.1	3600	HD 151680	03:18/05:24	1.2/1.0	360/720
SR 21	2010-06-05	05:49	1.0–1.3	3600	HD 151680	05:24/07:30	1.0/1.1–1.2	720/360
R CrA 7B	2010-06-05	08:39	1.1–1.4	3600	HD 169916	08:08	1.1	360
RXJ1615.3-3255	2010-06-18	01:55	1.0	1620	HD 149447	03:14	1.0	180
SSTc2dJ162145.1-234232	2010-07-10	03:23	1.1–1.2	1620	HD 139163	04:18	1.4	360
IRS 60	2010-07-10	4:58	1.3–1.6	1980	HD 151680	05:59	1.5	180
WL 19	2010-07-11	03:12	1.05–1.12	1620	HD 151680	04:08	1.1	180
WL 19	2010-07-11	04:56	1.3–1.6	1620	HD 151680	05:48	1.5	180
WL 20	2010-07-12	02:25	1.0–1.1	1980	HD 151680	03:27	1.1	180
V807 Tau	2010-12-25	02:52	1.5	1980	HD 28305	03:50	1.4	180
LkCa 15	2011-01-12	02:27	1.5	1620	HD 28305	01:52	1.4	180
LkCa 15	2011-01-12	03:30	1.6–1.8	1620	HD 28305	04:24	1.9	180

associated standard stars. Finally, the flux-calibrated spectrum is obtained by multiplying the observed spectrum of the star by a spectral response function. The response function is calculated by dividing the observed spectrum of a standard star by the flux model (at very low resolution and not including photospheric absorption lines) retrieved from the VISIR standard stars catalog. Photospheric absorption lines in the spectra of the standard stars have been eliminated by Gaussian fitting. This procedure allow us to correct both for sky transmission, which depends on the wavelength—because of telluric lines—and on the airmass, and for fringing, a flux modulation with the wavelength that is characteristic of VLT/VISIR spectra and that has been found to be constant over periods of several months (van Boekel et al. 2009). This procedure may not be very accurate if the signal-to-noise ratio of the standard is very low, if the airmass of the standard is different from the airmass of the target, or if the photospheric lines of the standard are not well subtracted, because they are blended with telluric lines. To verify that none of these sources of error affect our results, we derive our calibrated spectra using an alternative approach. Specifically, we remove the fringing and the telluric lines using a fringing model and a model of the atmosphere and, then, we used the standard stars only for the flux calibration. A more detailed discussion of this alternative method is reported in Pascucci et al. (2011).

The two methods for deriving the calibrated spectra give the same results for all the stars except for T CrA. In this case,

Table 3
Results

ID	Star	Flux (10^{-14} erg cm^{-2} s^{-1})	FWHM (km s^{-1})	v_{peak} (km s^{-1})	A_J (mag)	$L_{Ne\,II}$ (10^{28} erg s^{-1})	Flux (*Spitzer*) (10^{-14} erg cm^{-2} s^{-1})	References
1	V807 Tau	<1.1	...	...	0.2	<2.6	...	1 -
2	LkCa 15	<0.5	...	...	0.3	<1.2	0.28 ± 0.02	1 2
3	IRAS 08267-3336	<0.5	...	...	1.4	<13.8	1.40 ± 0.08	3 2
4	Hen 3-600 A	<0.2	...	...	0.2	<0.03	<0.5	4 2
5	WX Cha	<0.2	...	...	0.6	<0.03	0.57 ± 0.06	1 2
6	XX Cha	<0.2	...	...	0.3	<0.03	0.48 ± 0.02	1 2
7	T Cha	3.4 ± 0.3	44.9 ± 3.2	−10.5 ± 2.7	0.8	5.1 ± 0.5	3.20 ± 0.21	5 6
7	T Cha[a]	3.1 ± 0.2	39.4 ± 1.9	−4.7 ± 2.5	0.8	4.7 ± 0.3	3.20 ± 0.21	5 6
8	MP Mus	1.1 ± 0.1	15.9 ± 1.4	−4.4 ± 2.1	0.1	1.4 ± 0.2	<2.0	4 7
9	IM Lupi	<0.5	...	...	0.2	<1.4	1.07 ± 0.05	3 2
10	SZ 73	<0.6	...	...	0.8	<1.8	1.60 ± 0.24	8 6
10	Sz 73[a]	1.9 ± 0.2	72.8 ± 6.4	−97 ± 4	0.8	5.4 ± 0.6	1.60 ± 0.24	8 6
11	RU Lupi	2.4 ± 0.2(<0.3)[b]	106.7 ± 8.8	−168.2 ± 4.0	0.0	6.4 ± 0.7	2.60 ± 0.83	4 3
12	RX J1615.3-3255	1.4 ± 0.2	20.5 ± 2.7	−7.5 ± 2.8	0.3	3.8 ± 0.7	2.76 ± 0.46	9 2
13	SSTc2dJ162145.1	5.8 ± 0.5	44.1 ± 2.6	−18.0 ± 2.7	2.8	15.0 ± 1.2	11.83 ± 0.46	10 2
14	DoAr 25/GY92 17	<0.3	...	...	0.7	<0.5	0.50 ± 0.10	11 11
15	WL 10/GY92 211	<0.1	...	...	4.5	<0.4	1.60 ± 0.30	11 11
16	Elias 29/GY92 214	<0.5	...	...	11.4	<4.8	<8.5	11 11
17	SR 21	0.5 ± 0.1	15.1 ± 1.2	−8.3 ± 2.7	2.3	1.3 ± 0.1	<3.0	1 3
18	WL 19	<0.8	...	...	16.3	<15.2	<0.8	11 11
19	WL 20/GY92 240	<0.2	...	...	4.1	<0.7	6.28 ± 0.25	11 11
20	IRS 43/GY92 265 S	3.7 ± 0.3	37.5 ± 2.1	−6.2 ± 2.7	8.2	21.2 ± 1.5	45.30 ± 1.70	11 11
21	IRS 43/GY92 265 N	1.6 ± 0.2	35.7 ± 4.3	−7.6 ± 3.1	8.2	9.1 ± 1.4	45.30 ± 1.70	11 11
22	IRS 44/GY92 269	<0.7	...	...	12.8	<8.2	8.00 ± 2.40	11 11
23	IRS 45/GY92 273	0.6 ± 0.1	56.4 ± 6.4	−12.4 ± 3.7	6.6	2.9 ± 0.4	2.19 ± 0.41	11 11
24	IRS 47/GY92 279	<0.2	...	...	7.4	<1.0	2.01 ± 0.51	11 11
25	IRS 60/WSB 71a	0.9 ± 0.3(<0.2)[b]	49.4 ± 12.0	−54.9 ± 5.7	2.5	2.3 ± 0.8	1.91 ± 0.09	1 2
26	DoAr 44	<0.3	...	...	1.2	<0.5	...	10 -
27	V4046 Sgr	6.6 ± 0.2	22.5 ± 0.5	−10.5 ± 2.0	0.0	4.2 ± 0.1	7.68 ± 0.22	4 2
28	RX J1842.9-3532	<0.2	...	...	0.3	<0.5	0.43 ± 0.13	12 7
29	CrA IRS5 A	<0.6	...	...	7.0	<3.3	20.32 ± 0.65	13 2
30	CrA IRS5 B	<0.6	...	...	7.0	<3.1	20.32 ± 0.65	13 2
31	R CrA 7B	<0.5	...	...	26.0	<42.9	10.51 ± 0.42	13 2
32	T CrA	0.7 ± 0.2	19.1 ± 4.7	−2.0 ± 3.0	0.7	1.6 ± 0.5	8.88 ± 1.30	13 2

Notes. For the Ne II detections, fluxes, FWHMs, and the line peak velocities (v_{peak}) are calculated by fitting the spectrum with a Gaussian profile for the line and a first-order polynomial for the continuum. The line peak velocity is measured with respect to a reference system comoving with the star. Errors (1σ) are derived from the best-fit procedure. The Ne II luminosity is corrected for the extinction as discussed in the text. The last column reports the references for the A_J and the Ne II flux as measured from *Spitzer* low- and medium-resolution spectroscopy: (1) Furlan et al. 2009; (2) Curran et al. 2011; (3) Flaccomio et al. 2009; (4) Güdel et al. 2010; (5) Schisano et al. 2009; (6) Hughes et al. 1994; (7) Merín et al. 2010; (8) Evans et al. 2009; (9) Carpenter et al. 2008; (10) Forbrich & Preibisch 2007; (11) this work; (12) Lahuis et al. 2007; (13) Pascucci et al. 2007.

[a] Results obtained from a new reduction and calibration of the observations carried out by Pascucci & Sterzik 2009.

[b] Upper limit for a disk emission centered at 0 km s^{-1}.

the first procedure did not work very well because the airmass of the star and of the standard are different and because the equivalent width of the [Ne II] line is very low, so systematic errors associated with flux calibration turn out to be larger than statistical errors. On the basis of these considerations, for T CrA we applied the second procedure for the flux calibration.

Spitzer/IRS data for stars observed in the c2d survey were reduced using the c2d data reduction pipeline (see Lahuis et al. 2007 and Lahuis & Kessler-Silacci 2006 for further details). Data for other stars were downloaded from the Spitzer Heritage Archive in the basic calibrated data format processed with the S18.18.0 data pipeline. These data were analyzed using custom IDL code (including SSC software IRSCLEAN MASK) and the SMART (v.8.2.1.) program developed by the IRS Team at Cornell University (Higdon et al. 2004; Lebouteiller et al. 2010). To further improve the flux calibration, we reduced four spectra of the standard star ξ Draconis using the same procedure as for the science targets, and then we recalibrated the observed flux (the median among the four spectra) by using the median of these spectra and a model spectrum that has been produced by the MARCS code with the specific purpose of calibrating *Spitzer* spectra (Decin et al. 2004).

3. RESULTS

We observed 32 YSOs. Our targets belong to the star-forming regions Taurus, ρ Oph, Corona Australis, Lupus, and the Gum nebula, and to the nearby associations TW Hya, ϵ Cha, and β Pic.

Our results are summarized in Table 3. Fluxes, FWHMs, and peak velocities (v_{peak}) of the emission lines are calculated by fitting the spectral lines with the sum of a Gaussian and a constant continuum (see Figure 2). Errors (1σ) in the total flux and FWHMs are derived by a best-fit procedure. Systematic

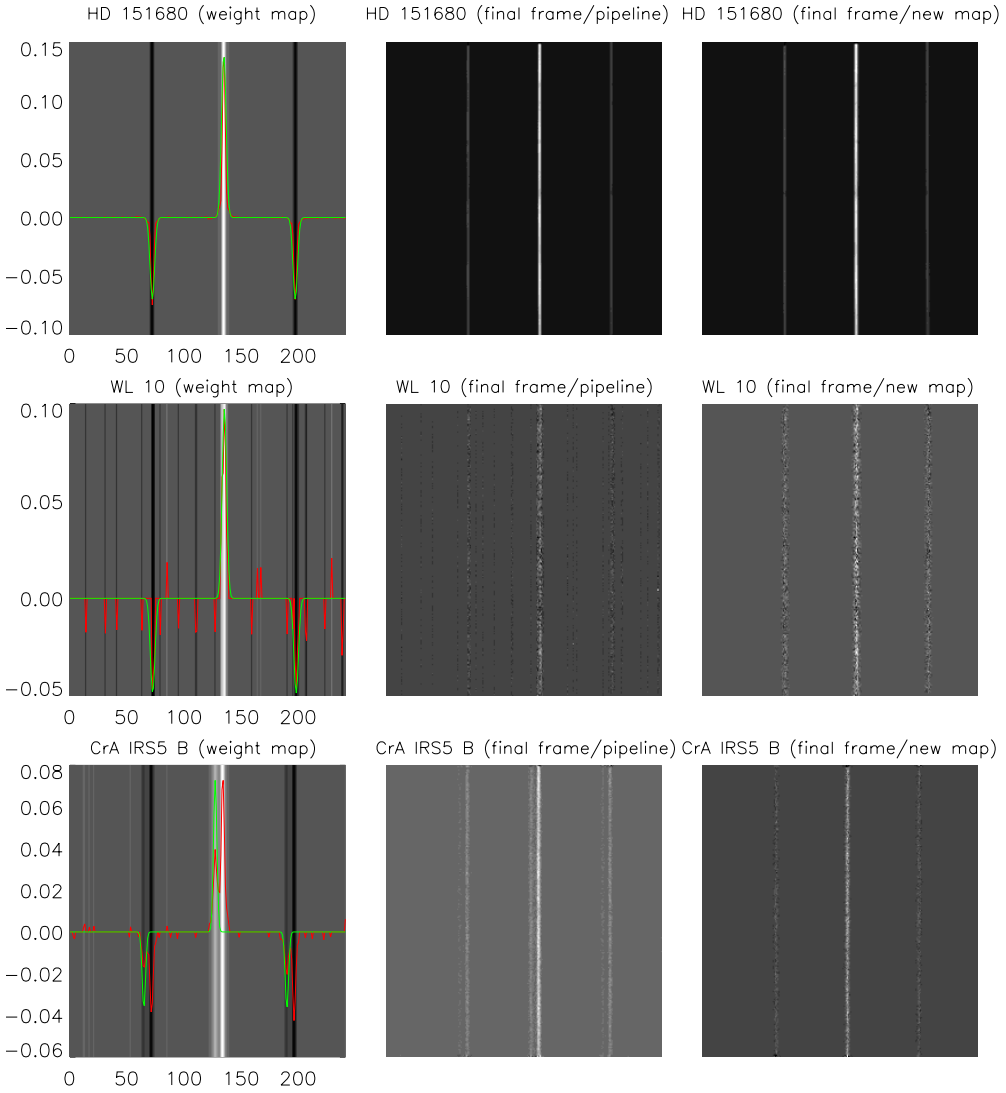

Figure 1. Examples of reduction of VISIR spectral image data. The left panels show weight maps calculated by the pipeline, while the central and the right panels show the final two-dimensional spectrum obtained by the pipeline and by an alternative data reduction using our own weight map, respectively. From top to bottom we show the frames for a very bright star (the standard HD 151680), a very faint star (WL 10), and a binary (CrA IRS 5), respectively. The red and the green lines overplotted on the left panels are the profiles along the spatial direction of the weight maps calculated from the pipeline (red line) and defined by us (green line). The two profiles are normalized to the same maximum value. On the *x*- and *y*-axes, we report the number of pixel and the intensity of the profile of the weight, respectively. For the binary, we show only the weight map for the secondary component.

(A color version of this figure is available in the online journal.)

errors associated with photometric calibration will be discussed later in this section. Errors on line peak velocities are the sum, in quadrature, of the statistical errors associated with the fitting procedure, the error on the stellar velocity reported in Table 1, and an additional error of 2 km s^{-1} that accounts for errors in positioning the star within the slit (see Pascucci et al. 2011 and Section 2.1). If in the observed wavelength range there are no significant emission features, we assume that the line has not been detected and we report the upper limit in Table 3. The upper limit depends on the assumed line width and was computed as $F_{\rm up} = 5\sigma_{\rm con}\sqrt{\rm FWHM\delta v}$, where $\sigma_{\rm con}$ is the standard deviation of the continuum emission, FWHM is the assumed full width at half-maximum of the line, and δv is the width of a velocity bin ($\sim$3.3 km s^{-1}). Upper limits reported in Table 3 are calculated for an assumed FWHM = 20 km s^{-1}. Four spectra of stars for which [Ne II] was not detected are shown in Figure 3 overplotted with a Gaussian with a total flux equal to the upper limit and an FWHM = 20 km s^{-1}. We chose to plot and report the upper limit for an assumed FWHM = 20 km s^{-1}, because it is the typical FWHM of the observed emission line produced by photoevaporative winds (see Section 4.2).

Even if standard stars were observed just after or before the science targets and were chosen as close as possible to the targets, a residual systematic error due to discrepancy between the airmass of the standard and of the target could affect our results. Pascucci et al. (2011) studied the systematic errors on VISIR observations of the [Ne II] emission by observing TW Hya several times during the same night. In their observations both flux and line peak velocity depended on the airmass. Specifically, the flux decreased up to a factor two as the airmass increased from 1 to 1.4, while the peak velocity varied from -4 to -7 km s^{-1}. In contrast, Pascucci et al. (2011) found that the observed FWHM of the line did not depend on the airmass.

All the detected lines are shown in Figure 2 with best-fit Gaussians overlaid on the data. All lines are well fitted by a Gaussian, except RU Lupi and IRS 43. Specifically, the emission

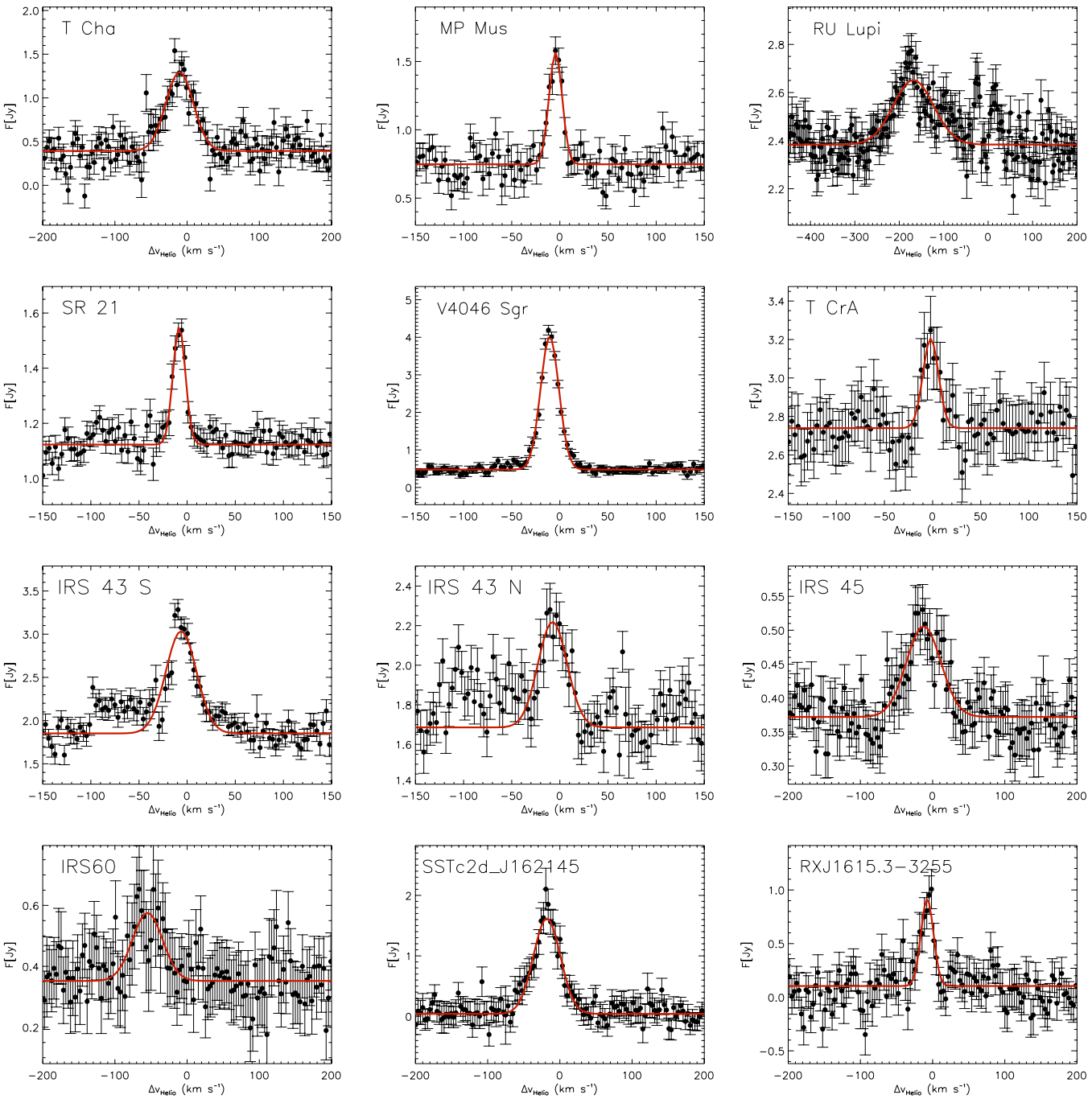

Figure 2. Flux-calibrated spectra of the 12 sources for which we detected the 12.81 μm [Ne II] emission line. The Gaussian best fit of the data is shown by the red curves. The spectra are plotted as a function of radial velocity in the stellocentric reference system.

(A color version of this figure is available in the online journal.)

of RU Lupi looks asymmetric, with the line peak blueshifted with respect to the line center; while in the spectra of both IRS 43 N and IRS 43 S we observe two features, a stronger one, which peaks very close to the stellar radial velocity and is well fitted by a Gaussian profile, and a weaker one, which is strongly blueshifted ($v_{\rm peak} \sim -100\,{\rm km\,s^{-1}}$) and asymmetric. However, this strongly blueshifted component is very weak and we are not sure if it is a real feature or a statistical fluctuation.

Two of our targets (Sz 73 and T Cha) have been previously observed by Pascucci & Sterzik (2009) using VISIR. To test our data reduction procedure and to compare our observations with the previous ones, we rereduced again the data obtained by Pascucci & Sterzik (2009), using our version of the pipeline. We obtained slightly higher fluxes in both cases; these are the values reported in Table 3. The new version of the pipeline performs a better subtraction of the sky that can influence the observed flux of very faint targets like T Cha and Sz 73. However, these discrepancies are not significant, so they do not influence the scientific results of either ours or previous analysis.

The two data sets for T Cha and Sz 73 also offer an opportunity to investigate variability of the [Ne II] line. In the case of T Cha the line flux, shape, and FWHM remained the same. On the contrary, in Sz 73 we failed to detect the [Ne II] from the outflow as previously reported in Pascucci & Sterzik (2009).

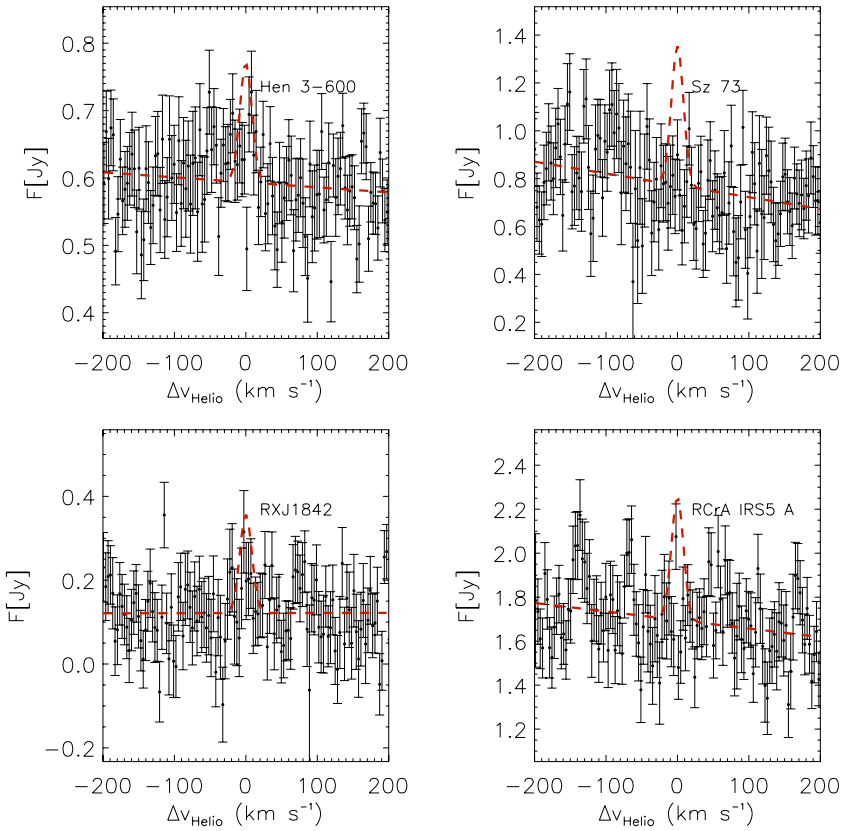

Figure 3. Flux-calibrated spectra of the four sources for which we did not detect the 12.81 μm [Ne II] emission line. Overplotted red lines show Gaussian profiles of a line with a total flux equal to the upper limit and an FWHM = 20 km s^{-1}. Radial velocities (x-axes) are with respect to the observed star as in Figure 2.
(A color version of this figure is available in the online journal.)

The second epoch data show upper limits of a factor 1.6 lower than the epoch one data (see Table 3). Because emission from Sz 73 is due to a protostellar jet, different slit orientations, different seeing or different positions of the star within the slit could produce significant discrepancies in the measured line flux. We can rule out the first two hypotheses because in the two observations the slit orientation on the plane of the sky was the same and the seeing was slightly better during the second observation when the line was not detected. Errors in centering the star within the slit or intrinsic variability could explain the discrepancy between the results of the two observations.

In Table 3, we also report line luminosities (or their upper limits) calculated from the distances reported in Table 1. We also consider the effect of the absorption from interstellar and circumstellar gas, which, at 12.81 μm, is not negligible for highly embedded sources, i.e., when the absorption in the J band is $A_J > 1$ mag (Flaccomio et al. 2009). Specifically, we obtained A_J (see Table 3) from the literature and, when it was not available, from measurement of optical extinction, using the conversion law $A_J = 0.282 A_V$ (Rieke & Lebofsky 1985), or from the absorption in the X-ray band ($N_{\rm H}$), using the conversion law $A_J = 1.8 \times 10^{-22} N_{\rm H}$ (Vuong et al. 2003). The absorption A_J is larger than 1 mag in 13 YSOs in ρ Ophiuchi, three sources in the Corona Australis, and only marginally ($A_J = 1.4$ mag) in IRAS 08267-3336. Chapman et al. (2009) showed that for highly absorbed stars in ρ Oph and other star-forming regions an extinction law with $R_V = 5.5$ is appropriate, as it accounts for grain growth in the dense part of the cloud. Therefore, for sources with $A_J > 1$, we calculate the absorption at 12 μm, using the relation $A_{12.81} = 0.16 A_J$ from Weingartner & Draine (2001), resulting in an absorption $A_{12.81}$ ranging from 0.22 to 4.16 mag. For all other sources, we used the standard $R_v = 3.1$ extinction law ($A_{12.81} = 0.097 A_J$ from Weingartner & Draine 2001). However, for these sources, the absorption has a negligible effect ($A_{12.81} < 0.1$ mag), independent of the extinction law used for the calculation.

In Table 3, we also report [Ne II] fluxes measured from spectra taken by *Spitzer*/IRS in the high-resolution mode ($R \sim 600$). We used values either reported from the literature or measured from archival data. For measuring line fluxes or their upper limits from *Spitzer* data, we used the same procedure as in Flaccomio et al. (2009). Specifically, we calculated the flux by integrating the emission between 12.78 and 12.84 μm and subtracting the underlying continuum by fitting a first- or a second-order polynomial in two adjacent spectral intervals (12.72–12.78 and 12.84–12.91 μm). In two cases (SSTc2dJ162145.13-234231.6 and RX J1615.3-3255) for which high-resolution spectra were not available, we used the low-resolution spectrum and different wavelength ranges to estimate the line flux (12.7–12.9 μm) and the continuum (12.3–12.7 and 12.9–13.3 μm). Upper limits (3σ) have been calculated, as previously discussed for VLT/VISIR data, from the rms on the continuum emission and assuming a fixed line width (0.023 μm).

4. DISCUSSION

We detected the [Ne II] line in 12 YSOs (3 Class I, 4 Class II, 4 transition disks, and 1 pre-transition disk); 11 of those are new detections with VISIR. We measured the FWHM and the velocity shift of all the detected lines. In Section 4.1, we compare

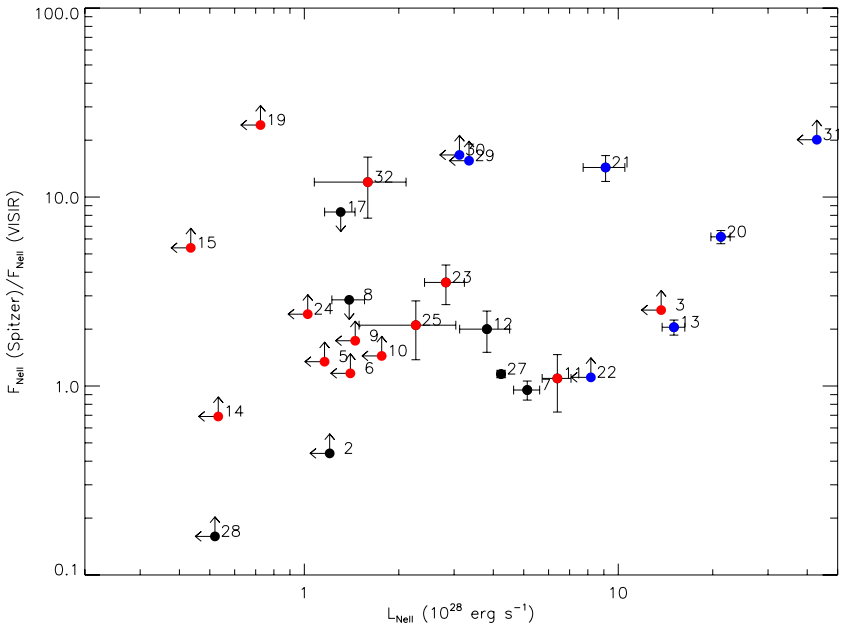

Figure 4. Ratio between flux of the [Ne II] line as measured from *Spitzer*/IRS and VLT/VISIR spectroscopic data as function of the [Ne II] luminosity measured from the VISIR data. Blue and red dots indicate Class I and Class II YSOs, respectively, while transition and pre-transitional disks are both indicated with black dots. For the two binary systems (IRS 43 and CrA IRS5) not resolved by *Spitzer*, but resolved by VISIR, we assumed that the [Ne II] emission observed by *Spitzer* was equally shared by the two components. Numbers are the IDs of the stars reported in Table 3.

(A color version of this figure is available in the online journal.)

fluxes of the [Ne II] line measured with VISIR and *Spitzer* and we discuss how discrepancies between observations with the two instruments can depend on the spatial location of the [Ne II] emitting gas. In Section 4.2, we compare all our results with other ancillary data (disk inclination, X-ray luminosity, and mass accretion rate) and irradiated disk models to better understand the physical mechanisms generating [Ne II] emission from gas within the inner disk.

4.1. Origin of the [Ne II] Emission

The aim of this work is to understand the origin of the [Ne II] emission in YSOs during the different phases of their evolution. Different emission mechanisms have been discussed in the literature. The [Ne II] emission could be a tracer of shocks produced by the interaction between a protostellar outflow and the interstellar medium (Hollenbach & McKee 1989; Hollenbach & Gorti 2009). This mechanism has been suggested to be at the origin of the emission observed from the triple system T Tau (van Boekel et al. 2009). The main observational evidence supporting this hypothesis is the spatial location of the emission: in fact, the emission is extended (1.″1) and located along the stellar outflow. Otherwise, the neon could be ionized by high-energy stellar emission. In this scenario the [Ne II] emission at 12.81 μm should be produced within the inner circumstellar disk, few AU from the central star. A handful of observations of transition disks support this second scenario by showing that the emission is usually compact and at a velocity close to that of the radial velocity of the central star (Herczeg et al. 2007; Najita et al. 2009; Pascucci & Sterzik 2009; Pascucci et al. 2011).

Information on the spatial distribution of the [Ne II] emission can be obtained by comparing fluxes measured by *Spitzer* (spatial resolution ∼4.″7) and VISIR (spatial resolution ∼0.″4). To illustrate this, we show in Figure 4 the ratio between the absorbed flux observed using *Spitzer* and VISIR as function of the [Ne II] absorption-corrected luminosity measured from the VISIR spectra for YSOs of various infrared classes. A systematic discrepancy is evident between the [Ne II] fluxes measured by *Spitzer* and VISIR for Class I YSOs (blue dots); namely, *Spitzer* fluxes range from 2 to more than 20 times larger than [Ne II] fluxes measured by VISIR, with the exception of one object, which might thus be compatible with the other Class I stars. This discrepancy strongly suggests that the [Ne II] emission observed from *Spitzer* in most Class I objects is spatially extended, i.e., it is not produced within the inner disk (r < 20–40 AU), but in the outer regions of the circumstellar envelope. Alternatively, the emission may span a very broad range of velocities, such that the upper limits reported in Table 3 could be underestimated (up to a factor five if we consider a line marginally resolved from *Spitzer*/IRS at high-resolution mode). However, both scenarios would suggest that neon in Class I objects is most likely ionized by shocks produced by protostellar outflows. To better investigate the [Ne II] emission from shocks located several AUs from the star, a different observational strategy is required. As previously done for T Tau by van Boekel et al. (2009), the position and the velocity structure of multiple knots composing a jet and emitting in the [Ne II] can be studied by performing several long-slit observations with different slit orientations to cover a large area around the target. Furthermore, to perform a complete study of the physical structure of protostellar jets, the results of these observations can be compared with narrowband imaging and spectroastrometric observations in other forbidden lines, like the [S II] doublet at 6717 and 6731 Å or the [O I] at 6300 Å.

On the other hand, in YSOs that are classified as transition or pre-transition disks (Tr and pTr in Table 1 and black dots in Figure 4), the ratio between [Ne II] fluxes measured by the two instruments is consistently less than 2, with the exception of two stars for which the upper limits might be compatible with other transition and pre-transition disks. For the three objects detected with both instruments, the ratio is consistent with 1

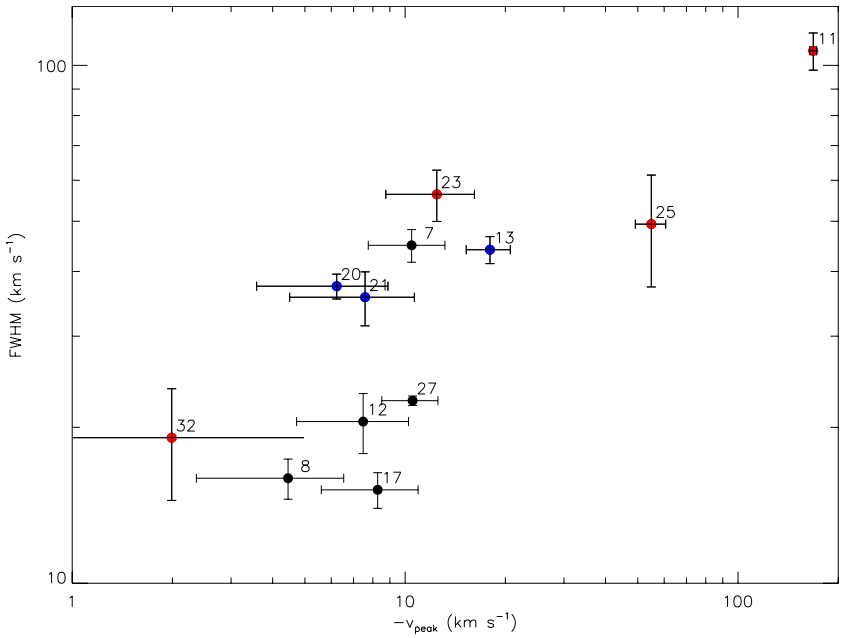

Figure 5. FWHM of the [Ne II] emission line as a function of the blueshift with respect to the stellar velocity. Colors of the symbols are as in Figure 4. Numbers are the IDs of the stars reported in Table 3.

(A color version of this figure is available in the online journal.)

at the 3σ confidence level. We conclude that, in transition and pre-transition disks, the bulk of the [Ne II] emission is produced within ~20–40 AU of the central star. In the next section, we will discuss whether this emission is due to a static disk atmosphere, a photoevaporative wind, or a magnetically accelerated outflow.

It is more complicated to interpret results for Class II YSOs, namely, stars harboring an optically thick disk. We detected the [Ne II] emission in four Class II YSOs. Since the ratio between *Spitzer* and VISIR fluxes ranges from ~1 to ~10, the spatially extended emission appears to be dominant, but significant emission from the inner disk may also be present.

4.2. *[Ne II] Emission from the Inner Region: Static Disk Atmosphere, Photoevaporative Wind, or Irradiated Protostellar Jet*

As discussed in the previous section, the detection of spatially unresolved [Ne II] emission in most of the transition and pre-transition disks demonstrates that the [Ne II] line is produced within the inner disk (less than 20–40 AU from the star), suggesting that neon is ionized by the high-energy emission from the central star. However, the emission may be produced by a static disk atmosphere, a photoevaporative wind (Alexander 2008; Ercolano & Owen 2010), or a magnetically accelerated outflow (Shang et al. 2010). The width and the velocity shift of the [Ne II] line at 12.81 μm should differ in these three cases. The emission from a static disk atmosphere should arise at the same mean radial velocity as the central star, with a broadening proportional to the disk inclination (e.g., the [Ne II] emission from GM Aur observed by Najita et al. 2009); whereas a photoevaporative wind—unless the disk has a large (~30 AU) inner disk hole (Ercolano & Owen 2010)—will produce blueshifted emission with respect to the central star (~1–10 km s^{-1}) and, again, a broadening proportional to the disk inclination. Blueshifted emission, very likely originating from a photoevaporative wind, has previously been observed in three transitional disks (T Cha, CS Cha, and TW Hydrae) by Pascucci & Sterzik (2009). Finally, the emission line from a magnetically driven outflow should be blueshifted to a larger velocity (~100 km s^{-1}) and much broader than emission from a disk, as observed, e.g., in Sz 73 by Pascucci & Sterzik (2009).

In Figure 5, we show the FWHMs of the detected lines as a function of their blueshifts with respect to the central star velocity. Colors represent the different infrared classes, as in Figure 4. Our results rule out the possibility that the [Ne II] emission is produced by a static disk atmosphere, since all of the detected lines are blueshifted with respect to the central star. In two of the stars of our sample (RU Lupi and IRS 60), the emission likely originates from a magnetically driven outflow, as demonstrated by the large blueshift ($v_{peak} = 168 \pm 4$ and $v_{peak} = 55 \pm 6$ km s^{-1}, respectively) and the large FWHM (107 ± 9 and 49 ± 12 km s^{-1}, respectively) of the observed emission lines. This hypothesis is confirmed by observational evidence that indicates that RU Lupi is the source of a well known protostellar jet (e.g., Takami et al. 2001), and by the proximity of IRS 60 to Herbig-Haro objects (Wu et al. 2002). Furthermore, the line profile of RU Lupi (top-right panel of Figure 2) appears slightly asymmetric, with the bluer part of the profile decreasing faster than the redder part. Similar asymmetric and strongly blueshifted profiles have been predicted by Shang et al. (2010), who modeled the [Ne II] emission produced by a magnetically accelerated wind irradiated by stellar high-energy emission. Unfortunately, the signal-to-noise ratio is too low to carry out a detailed comparison between our spectra and these models. In the spectra of IRS 43 N and IRS 43 S, we also observe a secondary emission component that is strongly blueshifted and asymmetric. However, although in each case the profile of this component resembles the profiles predicted by Shang et al. (2010), these highly blueshifted and asymmetric components from both IRS 43 N and IRS 43 S are too weak to establish if the resemblance is significant.

The emission observed from the other 10 YSOs is blueshifted by less than 18 km s^{-1}. For five of our targets, specifically

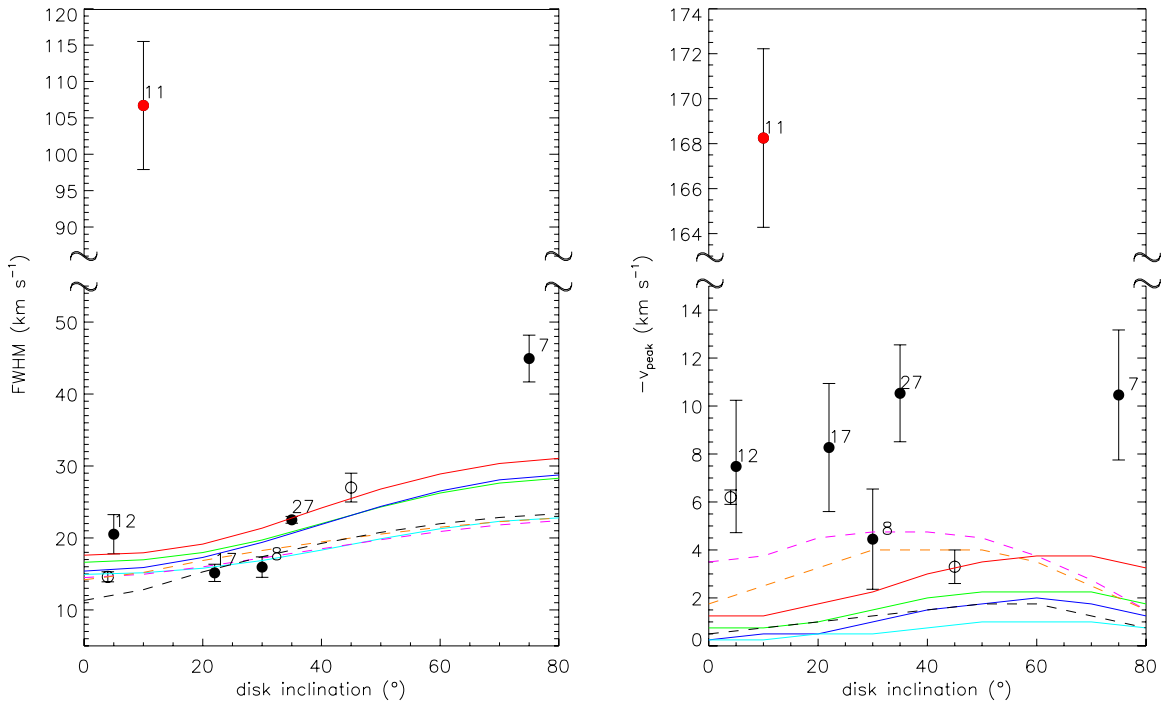

Figure 6. FWHM (left panel) and blueshift (right panel) of the [Ne II] emission as functions of the disk inclination. Empty symbols are from Pascucci & Sterzik (2009) and filled symbols are from this work. Colors of the symbols are as in Figure 4. In both panels, we overplot theoretical predictions from the models of Ercolano & Owen (2010). Specifically, red, green, blue, and cyan continuous lines were computed for transition disks irradiated by a star with X-ray luminosity $L_X = 2 \times 10^{30}$ erg s^{-1} and with an inner hole of 8.3, 14.2, 21.1, and 30.5 AU, respectively. Magenta, orange, and black dashed lines were computed for a primordial disk model without inner hole irradiated by a star with an X-ray luminosity of 2×10^{28}, 2×10^{29}, and 2×10^{30} erg s^{-1}, respectively. Numbers are the IDs of the stars reported in Table 3 (object 11 is RU Lupi).

(A color version of this figure is available in the online journal.)

transition and pre-transition disks, a disk origin is confirmed by the correlation between line FWHM and the disk inclination. The correlation is shown in the left panel of Figure 6, where we also plot two points from Pascucci & Sterzik (2009). In this panel, we also report the relation between FWHM and disk inclination derived from irradiated primordial and transition disk models by Ercolano & Owen (2010). Our measurements agree very well with the models, except in the case of RU Lupi and T Cha (the points on the top left and top right of the plot). In the first case, the emission is likely not due to a photoevaporative wind, but rather due to a magnetically accelerated outflow, as discussed above, so the models of Ercolano & Owen (2010) are not applicable. In the case of T Cha the discrepancy between models and observational data may be related to the difference between the mass of T Cha (1.3 $M_\odot$ from Schisano et al. 2009) and the mass of the central star assumed in the models (0.7 $M_\odot$). Discrepancies between the models and observations are more evident in the right panel of Figure 6, where we plot the line blueshift as a function of disk inclination. Specifically, the observed blueshifts are higher than the predicted ones. Higher blueshifts have been predicted by Alexander (2008), who considered a warmer disk atmosphere ($T \sim$ 10,000 K) irradiated by stellar EUV radiation.

For the other five YSOs with an observed blueshift of less than 18 km s^{-1} (IRS 43 N, IRS 43 S, IRS 45, SSTc2dJ162145.13-234231.6, and T CrA), the origin of the emission is less clear, because we do not know the disk inclination. Furthermore, four of these objects are in the earliest stage of the disk evolution (3 Class I IRS—43 N, IRS 43 S, and SSTc2dJ162145.13-234231.6—and a Class II—IRS 45) and the line FWHM is larger than observed in the transition disks, so the [Ne II] line at 12.81 μm could be produced by a jet seen with a large angle with respect to the line of sight. We also note that in these objects errors on the blueshift could be underestimated, because no radial velocities measurements are available in the literature, so we based our radial velocity estimate on the radial velocity of the parent cloud (ρ Ophiuchi) or other nearby stars (see Table 1). Observations aimed to measure accurate radial velocities and disk inclinations for these stars can help to distinguish between jet and disk origins.

In the left panel of Figure 7 we report the [Ne II] luminosity as a function of the X-ray luminosity, with the predictions of Ercolano & Owen (2010) overplotted with a dashed line. [Ne II] emission and X-ray luminosities do not appear correlated, as would be expected from the irradiated disk models (e.g., Meijerink et al. 2008, Ercolano & Owen 2010) and as has been observed by Güdel et al. (2010). However, the lack of a correlation between [Ne II] emission and X-ray luminosities could be due to the non-homogeneity of the observed sample. Specifically, our sample includes very different disks around stars of different masses that are going through different phases of the star formation process, while irradiated disk models that predict a correlation focused their analysis on a single prototypical disk. The relation between disk properties and predicted [Ne II] luminosity has been investigated by Schisano et al. (2010), who found that varying disk properties can cause luminosity variations up to one order of magnitude. Several upper limits in Figure 7 (left panel) lie below the [Ne II] luminosity predicted from the model of Ercolano & Owen (2010). The lack of detectable [Ne II] emission in Class I and Class II sources could depend on the effects of absorption on X-ray and EUV emission. Specifically, if EUV and X-ray

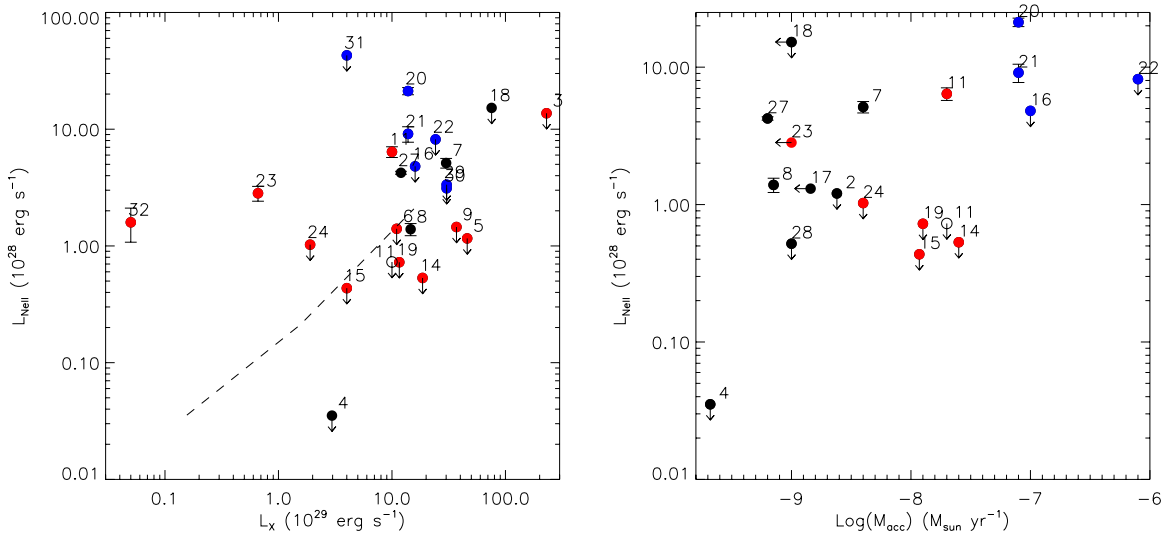

Figure 7. Luminosity in the [Ne II] line as a function of the X-ray luminosity in the 0.3–10 keV range (left panel) and mass accretion rate (right panel). Colors of the symbols are as in Figure 4, while the empty symbol shows the upper limit for RU Lupi for a second emission component located at zero velocity. The X-ray luminosity of the binary system IRS 43 has been assumed to be equally shared by the two components. The dashed line on the left panels represents the relation between [Ne II] and X-ray luminosity estimated from the irradiated disk models of Ercolano & Owen (2010). Numbers are the IDs of the stars reported in Table 3.

(A color version of this figure is available in the online journal.)

emission are strongly attenuated by the optically thick inner disk layers, the amount of ionized neon could be less than predicted by the models. In transition disks—like Hen 3-600, for which the upper limit on the [Ne II] luminosity is one order of magnitude below the expected value—the discrepancy between model and observations may be attributed to the opposite reason; namely, some of these disks have lost a large part of their circumstellar gas, so we do not see strong emission lines in the mid-infrared. In the case of Hen 3-600, a non-detection of [Ne II] emission is consistent both with the lack of detection of molecular CO emission (Andrews et al. 2010) and its low mass accretion rate (see Table 1). In contrast, higher mass accretion rates and strong molecular CO emission (see Kastner et al. 1997, 2008, 2010; Curran et al. 2011) characterize TW Hya, V4046 Sgr, and MP Mus where a strong [Ne II] emission was detected. Another possibility is that neon is ionized by EUV or soft X-ray photons mainly produced by accretion shocks, hence the line emission at 12.81 μm strongly decreases at low mass accretion rates.

The right panel of Figure 7 shows a weak correlation between [Ne II] luminosity and mass accretion rate, but this correlation is strongly influenced by just three objects (RU Lupi, IRS 43 N, and IRS 43 S). As discussed above, the [Ne II] emission in RU Lupi is produced by a protostellar jet, while the origin of the emission from IRS 43 N and IRS 43 S is uncertain. So, as suggested by Flaccomio et al. (2009) and Güdel et al. (2010), the correlation between [Ne II] luminosity and mass accretion rate may be driven by the presence of strong emission from jet sources, which are typically strong accretors.

5. SUMMARY AND CONCLUSIONS

We observed 32 YSOs belonging to different infrared classes using the high-resolution ($R \sim 30{,}000$) mid-infrared spectrograph VISIR at the VLT, with the aim of studying the origin of the [Ne II] emission line at 12.81 μm. We detected the line in 12 YSOs, thus tripling the number of detections of 12.81 μm [Ne II] emission in YSOs at high spectral resolution. We also collected from the literature published *Spitzer*/IRS data for 14 of our targets and analyzed archival data for another 14 stars. By comparing VLT/VISIR and *Spitzer*/IRS data with ancillary data retrieved from the literature, we obtained the following results.

1. Comparison between VISIR (slit width 0.″4) and IRS (slit width ∼4.″7) fluxes demonstrates that for Class I YSOs the [Ne II] emission is mainly produced by gas located at a distance of more than 20–40 AU (i.e., outside of the VISIR slit but within the IRS slit) from the central star and, therefore, arises from the extended envelopes. At these distances from the star, neon is most likely ionized by energetic shocks produced from protostellar outflows.
2. The same comparison (VISIR versus IRS) shows that the [Ne II] emission from transition and pre-transition disks is produced by gas located within a few AU from the central stars, while in Class II objects we observe emission both from the inner region and from the extended envelope.
3. Observed blueshifts and FWHMs of the [Ne II] line are consistent with emission in either a photoevaporative wind or the launching region of magnetically driven outflow. We associated the emission with a photoevaporative wind in five pre-main-sequence stars with transition and/or pre-transition disks (blueshifts between 2 and 18 km s^{-1}, FWHM between 15 and 45 km s^{-1}), where we observe a correlation between line FWHM and disk inclination. Otherwise, we associated the emission to an outflow in two objects (blueshifts of 55 and 168 km s^{-1}, FWHM of 49 and 107 km s^{-1}), one of which, RU Lupi, is a prototypical target for studies of protostellar jets. The origin of the emission in the remaining five objects is more uncertain.
4. We compared the dependence of line FWHM and blueshift on disk inclinations with the predictions of irradiated disk models of Ercolano & Owen (2010). The observed relation between line FWHM and disk inclination is consistent with the predictions of models, except for a single star (T Cha) whose disk is seen at high inclination angle. Line blueshifts are larger than predictions from the models.

Blueshifted emission and a correlation of the line width with disk inclination have been also predicted in the

case of photoevaporative wind triggered by EUV radiation (Alexander 2008).

5. We detected [Ne II] emission with blueshifts smaller than $\sim$20 km s^{-1} from three Class I objects and two Class II objects. Although these projected velocities appear small for an outflow origin, and would rather point toward a disk wind, we have no constraints on the inclinations of these systems and thus on the true velocity of the emitting material.

Our observations demonstrate that the [Ne II] emission in YSOs arises either from shocks formed in protostellar jets or from a photoevaporative wind in the inner disk, and high spatial and spectral resolution observations are necessary to distinguish between the two mechanisms. Specifically, the former mechanism prevails in early stages of the star formation process when powerful outflows are generated, while the latter prevails in the latest stages of disk evolution. However, to understand whether the two processes may coexist and photoevaporative winds are already active at early stages, a better knowledge of disk properties (i.e., disk inclination, radial velocities, and disk structure) is required. The new instruments operating in mid-infrared and submillimeter band (VLT/CRIRES, Herschel, ALMA) will allow us to better study these systems and interpret our results.

For what concerns the more evolved transition and pre-transition disks, the presence of emission blueshifted of $\sim$2–10 km s^{-1} and the correlation between line width and disk inclination are strong evidence for the photoevaporation from the disk. However, observations in the [Ne II] line are not sufficient to understand the full physical scenario, specifically, it is not clear if EUV emission produced by accretion shocks or X-rays produced either by accretion shocks or coronae is the main driver of photoevaporation and disk heating. High spectral resolution observations of other forbidden emission lines (e.g., [O I] at 6300 Å; Pascucci et al. 2011) emitted in the inner disk region may help to address this issue.

Finally, we detected the [Ne II] line in only 13 YSOs out of the 32 observed. This is not surprising given that upper limits are in many cases of the same order of magnitude of the expected luminosity (see the left panel of Figure 7). Therefore, our study is biased toward stronger and closer sources. A higher sensitivity instrument is required to observe a larger and more complete sample and thereby to fully explore the space of physical parameters of the star–disk system. The upgraded VLT/VISIR expected in the next summer will be a first step in this direction.

This publication makes use of data products from the Two Micron All Sky Survey, which is a joint project of the University of Massachusetts and the Infrared Processing and Analysis Center/California Institute of Technology, funded by the National Aeronautics and Space Administration and the National Science Foundation. This work is based in part on observations made with the *Spitzer Space Telescope*, obtained from the NASA/IPAC Infrared Science Archive, both of which are operated by the Jet Propulsion Laboratory, California Institute of Technology, under a contract with the National Aeronautics and Space Administration. We thank Dan Dicken for his help with the data reduction of *Spitzer* high-resolution spectra. This research was supported in part by NASA Astrophysics Data Analysis Program and National Science Foundation grants (grant numbers NNX09AC96G and AST–1108950, respectively) to RIT. I.P. acknowledges support from NSF Astronomy & Astrophysics research (ID AST0908479).

Facilities: VLT:Melipal, *Spitzer*

REFERENCES

Alexander, R. D. 2008, MNRAS, 391, L64
Andrews, S. M., Czekala, I., Wilner, D. J., et al. 2010, ApJ, 710, 462
Andrews, S. M., Wilner, D. J., Hughes, A. M., Qi, C., & Dullemond, C. P. 2009, ApJ, 700, 1502
Argiroffi, C., Maggio, A., Peres, G., et al. 2009, A&A, 507, 939
Argiroffi, C., et al. 2011, ApJ, submitted
Brown, J. M., Blake, G. A., Dullemond, C. P., et al. 2007, ApJ, 664, L107
Carpenter, J. M., Bouwman, J., Silverstone, M. D., et al. 2008, ApJS, 179, 423
Carr, J. S., & Najita, J. R. 2008, Science, 319, 1504
Chapman, N. L., Mundy, L. G., Lai, S.-P., & Evans, N. J., II 2009, ApJ, 690, 496
Comerón, F. 2008, in Handbook of Star Forming Regions, Vol II: The Southern Sky, ed. B. Reipurth (San Francisco, CA: ASP), 295
Cortes, S. R., Meyer, M. R., Carpenter, J. M., et al. 2009, ApJ, 697, 1305
Covey, K. R., Greene, T. P., Doppmann, G. W., & Lada, C. J. 2006, AJ, 131, 512
Curran, R. L., Argiroffi, C., Sacco, G. G., et al. 2011, A&A, 526, A104
Decin, L., Morris, P. W., Appleton, P. N., et al. 2004, ApJS, 154, 408
Doppmann, G. W., Jaffe, D. T., & White, R. J. 2003, AJ, 126, 3043
Dutrey, A., Guilloteau, S., & Guelin, M. 1997, A&A, 317, L55
Dutrey, A., Guilloteau, S., & Simon, M. 1994, A&A, 286, 149
Eisner, J. A., Monnier, J. D., Tuthill, P., & Lacour, S. 2009, ApJ, 698, L169
Ercolano, B., Clarke, C. J., & Drake, J. J. 2009, ApJ, 699, 1639
Ercolano, B., Drake, J. J., Raymond, J. C., & Clarke, C. C. 2008, ApJ, 688, 398
Ercolano, B., & Owen, J. E. 2010, MNRAS, 406, 1553
Espaillat, C., Calvet, N., D'Alessio, P., et al. 2007a, ApJ, 670, L135
Espaillat, C., Calvet, N., D'Alessio, P., et al. 2007b, ApJ, 664, L111
Espaillat, C., D'Alessio, P., Hernández, J., et al. 2010, ApJ, 717, 441
Evans, N. J., Dunham, M. M., Jørgensen, J. K., et al. 2009, ApJS, 181, 321
Flaccomio, E., Stelzer, B., Sciortino, S., et al. 2009, A&A, 505, 695
Forbrich, J., & Preibisch, T. 2007, A&A, 475, 959
Furlan, E., Watson, D. M., McClure, M. K., et al. 2009, ApJ, 703, 1964
Glassgold, A. E., Najita, J. R., & Igea, J. 2007, ApJ, 656, 515
Güdel, M., Lahuis, F., Briggs, K. R., et al. 2010, A&A, 519, A113
Guenther, E. W., Esposito, M., Mundt, R., et al. 2007, A&A, 467, 1147
Hartmann, L. W., Soderblom, D. R., & Stauffer, J. R. 1987, AJ, 93, 907
Herczeg, G. J., Najita, J. R., Hillenbrand, L. A., & Pascucci, I. 2007, ApJ, 670, 509
Higdon, S. J. U., Devost, D., Higdon, J. L., et al. 2004, PASP, 116, 975
Hollenbach, D., & Gorti, U. 2009, ApJ, 703, 1203
Hollenbach, D., & McKee, C. F. 1989, ApJ, 342, 306
Horne, K. 1986, PASP, 98, 609
Houck, J. R., Roellig, T. L., van Cleve, J., et al. 2004, ApJS, 154, 18
Huenemoerder, D. P., Kastner, J. H., Testa, P., Schulz, N. S., & Weintraub, D. A. 2007, ApJ, 671, 592
Hughes, A. M., Andrews, S. M., Wilner, D. J., et al. 2010, AJ, 140, 887
Hughes, J., Hartigan, P., Krautter, J., & Kelemen, J. 1994, AJ, 108, 1071
Kastner, J. H., Hily-Blant, P., Sacco, G. G., Forveille, T., & Zuckerman, B. 2010, ApJ, 723, L248
Kastner, J. H., Zuckerman, B., Hily-Blant, P., & Forveille, T. 2008, A&A, 492, 469
Kastner, J. H., Zuckerman, B., Weintraub, D. A., & Forveille, T. 1997, Science, 277, 67
Kenyon, S. J., Dobrzycka, D., & Hartmann, L. 1994, AJ, 108, 1872
Lagage, P. O., Pel, J. W., Authier, M., et al. 2004, Messenger, 117, 12
Lahuis, F., & Kessler-Silacci, J. E. 2006, c2d Spectroscopy Explanatory Supplement (Pasadena, CA: Spitzer Science Center)
Lahuis, F., van Dishoeck, E. F., Blake, G. A., et al. 2007, ApJ, 665, 492
Lebouteiller, V., Bernard-Salas, J., Sloan, G. C., & Barry, D. J. 2010, PASP, 122, 231
Lombardi, M., Lada, C. J., & Alves, J. 2008, A&A, 489, 143
Lundin, K. L. 2008, VLT VISIR Pipeline User Manual (Garching: ESO)
Manoj, P., Kim, K. H., Furlan, E., et al. 2011, ApJS, 193, 11
Meijerink, R., Glassgold, A. E., & Najita, J. R. 2008, ApJ, 676, 518
Melo, C. H. F. 2003, A&A, 410, 269
Merín, B., Brown, J. M., Oliveira, I., et al. 2010, ApJ, 718, 1200
Najita, J. R., Doppmann, G. W., Bitner, M. A., et al. 2009, ApJ, 697, 957
Natta, A., Testi, L., & Randich, S. 2006, A&A, 452, 245
Neuhäuser, R., & Forbrich, J. 2008, in Handbook of Star Forming Regions, Vol. II: The Southern Sky, ed. B. Reipurth (San Francisco, CA: ASP), 735
Neuhäuser, R., Walter, F. M., Covino, E., et al. 2000, A&AS, 146, 323
Owen, J. E., Ercolano, B., Clarke, C. J., & Alexander, R. D. 2010, MNRAS, 401, 1415
Pascucci, I., Hollenbach, D., Najita, J., et al. 2007, ApJ, 663, 383
Pascucci, I., & Sterzik, M. 2009, ApJ, 702, 724

Pascucci, I., Sterzik, M., Alexander, R. D., et al. 2011, ApJ, 736, 13
Pettersson, B. 2008, in Handbook of Star Forming Regions, Vol. II: The Southern Sky, ed. B. Reipurth (San Francisco, CA: ASP), 43
Pinte, C., Padgett, D. L., Ménard, F., et al. 2008, A&A, 489, 633
Quast, G. R., Torres, C. A. O., de La Reza, R., da Silva, L., & Mayor, M. 2000, in IAU Symp. 200, The Formation of Binary Stars, ed. B. Reipurth & H. Zinnecker (Cambridge: Cambridge Univ. Press), 28
Rieke, G. H., & Lebofsky, M. J. 1985, ApJ, 288, 618
Salyk, C., Pontoppidan, K. M., Blake, G. A., et al. 2008, ApJ, 676, L49
Schegerer, A. A., Wolf, S., Hummel, C. A., Quanz, S. P., & Richichi, A. 2009, A&A, 502, 367
Schisano, E., Covino, E., Alcalá, J. M., et al. 2009, A&A, 501, 1013
Schisano, E., Ercolano, B., & Güdel, M. 2010, MNRAS, 401, 1636
Schütz, O., Meeus, G., Sterzik, M. F., & Peeters, E. 2009, A&A, 507, 261
Shang, H., Glassgold, A. E., Lin, W., & Liu, C. 2010, ApJ, 714, 1733
Skrutskie, M. F., Cutri, R. M., Stiening, R., et al. 2006, AJ, 131, 1163
Smette, A., & Vanzi, L. 2007, VISIR User Manual (Garching: ESO)
Stempels, H. C., & Piskunov, N. 2002, A&A, 391, 595
Takami, M., Bailey, J., Gledhill, T. M., Chrysostomou, A., & Hough, J. H. 2001, MNRAS, 323, 177
Torres, C. A. O., Quast, G. R., da Silva, L., et al. 2006, A&A, 460, 695
Torres, C. A. O., Quast, G. R., Melo, C. H. F., & Sterzik, M. F. 2008, in Handbook of Star Forming Regions, Vol. II: The Southern Sky, ed. B. Reipurth (San Francisco, CA: ASP), 757
Uchida, K. I., Calvet, N., Hartmann, L., et al. 2004, ApJS, 154, 439
van Boekel, R., Güdel, M., Henning, T., Lahuis, F., & Pantin, E. 2009, A&A, 497, 137
Vuong, M. H., Montmerle, T., Grosso, N., et al. 2003, A&A, 408, 581
Wang, H., Mundt, R., Henning, T., & Apai, D. 2004, ApJ, 617, 1191
Weingartner, J. C., & Draine, B. T. 2001, ApJ, 548, 296
Werner, M. W., Roellig, T. L., Low, F. J., et al. 2004, ApJS, 154, 1
Wichmann, R., Covino, E., Alcalá, J. M., et al. 1999, MNRAS, 307, 909
Williams, J. P., & Cieza, L. A. 2011, ARA&A, 49, 67
Wu, J., Wang, M., Yang, J., Deng, L., & Chen, J. 2002, AJ, 123, 1986
Yamada, C., Kanamori, H., & Hirota, E. 1985, J. Chem. Phys., 83, 552